# Driving a conceptual model climate by different processes: Snapshot attractors and extreme events

Tamás Bódai,[1,2] György Károlyi,[3] and Tamás Tél[4]
[1]*KlimaCampus, Institute of Meteorology, University of Hamburg, Grindelberg 5, D-20144 Hamburg, Germany*
[2]*Max Planck Institute for the Physics of Complex Systems, Nöthnitzer Strasse 38, D-01187 Dresden, Germany*
[3]*Institute of Nuclear Techniques, Budapest University of Technology and Economics, Műegyetem rkp. 9., H-1111 Budapest, Hungary*
[4]*Institute for Theoretical Physics–Hungarian Academy of Sciences Research Group, Eötvös University, Pázmány P. s. 1/A, H-1117 Budapest, Hungary*
(Received 30 October 2012; published 28 February 2013)

In a low-order chaotic model of global atmospheric circulation the effects of driving, i.e., time-dependent (periodic, chaotic, and noisy) forcing, are investigated, with particular interest in extremal behavior. An approach based on snapshot attractors formed by a trajectory ensemble is applied to represent the time-dependent likelihood of extreme events in terms of a physical observable. A single trajectory-based framework, on the other hand, is used to determine the maximal value and the kurtosis of the distribution of the same observable. We find the most significant effect of the driving on the magnitude, relative frequency, and variability of extreme events when its characteristic time scale becomes comparable to that of the model climate. Extreme value statistics is pursued by the method of block maxima, and found to follow Weibull distributions. Deterministic drivings result in shape parameters larger in modulus than stochastic drivings, but otherwise strongly dependent on the particular type of driving. The maximal effects of deterministic drivings are found to be more pronounced, both in magnitude and variability of the extremes, than white noise, and the latter has a stronger effect than red noise.

DOI: 10.1103/PhysRevE.87.022822 PACS number(s): 05.45.−a, 05.40.−a

## I. INTRODUCTION

The concept of climate has attracted the interest of great scientists [1]. It is commonly defined as the collection of some long-time average temperature, humidity, precipitation, etc. (see the Glossary of the 2007 Synthesis Report of the IPCC [2]). *Alternatively*, the average (or other statistical measures in a wider sense) can be taken over an *ensemble* of possible states stemming from unknown initial conditions in the distant past of a dissipative system [3–7]. Thus, climate in the latter theoretical sense is independent of initial conditions and governed only by forcing. In dynamical systems terms the concept of *pullback* [8] or *snapshot attractor* [9], arising in the study of driven nonautonomous systems, coincides precisely with the ensemble that is referred to in the above alternative definition of climate. A snapshot attractor is an object which is approximated by trajectories initialized in the infinitely distant past, while all of them experience the *same* perturbations. With chaotic dynamics the snapshot attractor is a fractal, whose shape changes over time, but its fractal dimension is constant [9,10]. A rigorous mathematical definition of the pullback attractor of a nonautonomous dynamical system can be given in terms of its two-time evolution operator [11,12].

The method of stochastic parametrization [3,13], in order to account for physically unmodeled subgrid scale processes in complex climate models in an efficient and manageable way, naturally leads to the studying of driven dynamics. Furthermore, a planetary climate dominated by solar radiation or climate subsystems, embedded in a network of subsystems, can be seen as genuinely driven. It has been proposed [12,14] that snapshot attractors, being the building blocks of the fuzzy chaotic attractors arising in the traditional approach [15], can provide additional geometric information about the driven dynamics, potentially much more rich than the undriven one [5].

In earlier papers [5,16] we extended the white noise-driven snapshot attractor approach of climate-related problems to chaotic and periodic drivings. With a chaotic driving [16] of variable time scale we found typically an enhancement of the magnitude of extremes, the strongest effect occurring for the time scale comparable to that of the undriven system.

Here we expand on our study of the effects of the variable time scale of drivings. Beside deterministic chaotic drivings, for a comparison, we consider red noise as a stochastic process, and, for reference, we also consider the highly regular periodic signal and the completely irregular, uncorrelated white noise. For a listing and classification of processes to be used as driving, see Fig. 1.

To demonstrate the effects of such drivings, a conceptual climate model described by three ordinary differential equations is analyzed: Lorenz's (L84) model of global atmospheric circulation [17]. Such simple models play an important role in climate research [18], as they expedite efficient testing of theoretical ideas, and facilitate simple visualization of the results.

Both within the snapshot attractor- and the single trajectory-based frameworks our analysis shows that the magnitude, relative frequency, and variability of extremes is maximally enhanced when the time scale of driving becomes comparable with that of the undriven climate system—indicating a resonancelike effect. With more regular drivings, exhibiting a higher degree of periodicity, the effects are more enhanced.

Different choices of the type of the driving process will be explored also in terms of a more comprehensive extreme value statistics. Extreme value statistics in dynamical systems have been concerned exclusively with autonomous *undriven* systems so far (see, e.g., Refs. [19–23]), and here we apply the standard method of block maxima to driven dynamical systems. For all types of drivings Weibull distributions are found, with shape parameters larger in modulus for deterministic as opposed to stochastic drivings, but otherwise strongly dependent on the particular type of driving.

In the following section the L84 model is described, along with the various processes that are used as driving. In Sec. III the concept of snapshot attractors is introduced in more

 

| | P | R | L | C | W |
|---|---|---|---|---|---|
| Variable time scale | | | | | |
| Time-continuous | | | | | |
| Deterministic | | | | | |
| Regular | | | | | |

FIG. 1. List of processes to be used to drive a conceptual climate model (L84): (P) Periodic signal, (R) first component of the Rössler equations, (L) first component of the classical Lorenz equations, (C) red (colored) noise, (W) white noise. (See Sec. II.) Some properties of the processes are indicated (dense hatches for affirmative, blank for the opposite). The loose hatches indicate partial validity of the property in question.

detail, examples are given, and measures of certain regions of the snapshot attractor are associated with extreme events. Section IV provides a systematic numerical comparative study by varying the time scale of different drivings, demonstrating possible enhancement of magnitude and variability of extremes. An interpretation of these findings is given based on the periodically driven case. Extreme value statistics is pursued in Sec. V, whereby the shape parameter of the prevailing extreme value distribution is determined using the method of block maxima. In Sec. VI we draw conclusions on the effects of driving on various properties.

## II. MODEL AND DRIVINGS

Lorenz's model of global atmospheric circulation (L84) reads as follows [17,18]:

$$\begin{aligned} \dot{x} &= -y^2 - z^2 - ax + aF, \\ \dot{y} &= xy - bxz - y + 1, \\ \dot{z} &= xz + bxy - z. \end{aligned} \tag{1}$$

These equations express the fact that within the atmospheric dynamics, which is fundamentally determined by solar forcing, wind energy might drive a heat transport towards the pole, facilitated by cyclones that are given rise by a global instability, called the baroclinic instability. The thermal imbalance due to solar forcing, related to averaged wind speeds of the Westerlies, is represented by variable $x$. Two modes of the cyclonic oscillations are represented by their amplitudes, $y$ and $z$. The total cyclonic activity can be described by the composed variable

$$r = \sqrt{y^2 + z^2}. \tag{2}$$

The total energy of the model atmosphere $E = (x^2 + y^2 + z^2)/2$ is varying but bounded.

For the parameter setting we take the common choice: $a = 1/4$, $b = 4$. Parameter $a$ is the ratio of the damping times of the Westerlies and the cyclonic eddies, while $b$ is the ratio of relaxation times of the displacement and amplification of eddies by the Westerlies. The equations appear in a dimensionless form with the time unit corresponding to about 5 days.

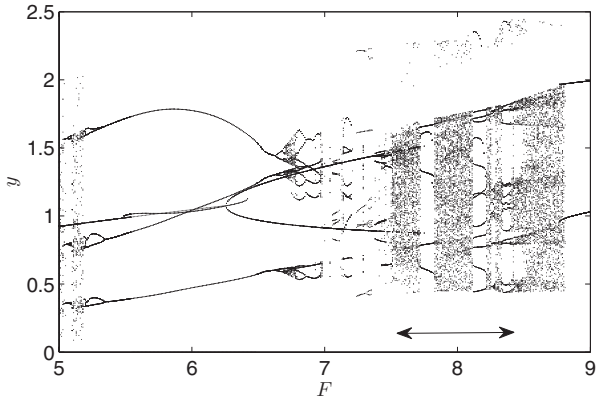


FIG. 2. Bifurcation diagram $y$ vs $F$, using several long trajectories sectioned by a Poincaré surface (see main text). All coexisting attractors are represented. A double arrow indicates the approximate range of drivings, corresponding to coupling strengths ($A$) given in the caption of Fig. 4.

The dynamics of L84 is determined by the strength $F$ of the solar irradiation. For, e.g., $F \equiv 6$ or $F \equiv 8$ a regular summer or a chaotic winter is found; see the bifurcation diagram in Fig. 2. The dynamics can be conveniently visualized by a two-dimensional (2D) Poincaré section (PS) of the attractor. The sectioning surface $z = 0$ with $\dot{z} > 0$ is a suitable choice for this. Figure 4(f) shows the PS of the chaotic winter attractor. The characteristic time of the L84 dynamics for $F \equiv 8$ turns out to be about 20 days. The dimensionless L84 time is thus $\tau_{\mathrm{L84}} = 4$.

Driving of L84 is introduced through a time-dependent term in the solar forcing, which fluctuates around a mean value $F_0$:

$$F = F(t) = F_0 + \Delta F(t). \tag{3}$$

The fluctuations $\Delta F(t)$ may be interpreted as the variation of the albedo via various mechanisms. Examples may include cloud formation due to varying weather conditions of convectional origin, or orbital eccentricity. The dimensionless characteristic time $\tau$ of $\Delta F(t)$, given in *multiples* of $\tau_{\mathrm{L84}}$, are in these cases $\tau \leqslant 1$ and $\tau \gg 1$, respectively. More generally, $F(t)$ can also be considered as the strength of the green house effect.

In this paper we use $F_0 = 8$ [corresponding to the Lorenzian winter scenario with $\Delta F(t) = 0$]. To characterize the driving, defined as

$$\Delta F(t) = A[\tilde{x}(t) - \langle \tilde{x}(t) \rangle],$$

five different processes, $\tilde{x}(t)$, will be considered. $\langle \tilde{x}(t) \rangle$ represent the long-time average of the process. With coupling strength $A$ the magnitude of the driving can be controlled.

(P) *Periodic* driving:

$$\tilde{x} = \sin(2\pi t/\tau_P). \tag{4}$$

This regular driving serves as a reference. Its frequency spectrum in Fig. 3(a) features a characteristic peak at $f = 1/\tau_P$. That is, the characteristic time (compared to that of L84) is $\tau = \tau_P/\tau_{\mathrm{L84}} = \tau_P/4$, which is to be varied for our analysis.

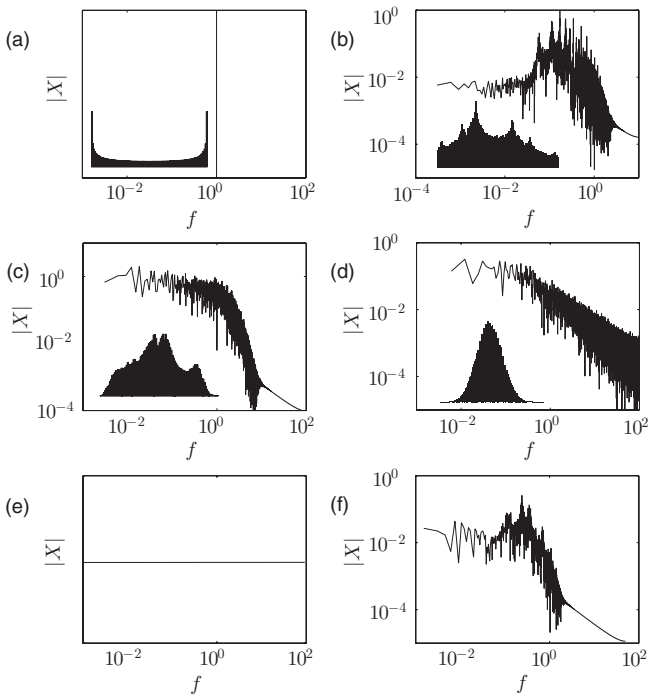


FIG. 3. Frequency spectra $|X| = |X(f)|$ [absolute value of the Fourier transform as a function of the (nondimensional) frequency $f$] of the various processes $\tilde{x}(t)$ that are used to drive L84 (see code names in Fig. 1 or the main text): (a) P, (b) R, (c) L, (d) C, (e) W, and (f) that of $x$ of the undriven L84. They are shown in log-log diagrams to indicate possible power law behavior. In the case of periodic driving a Dirac delta is represented by a vertical line, and in the case of white noise a horizontal line indicates the uniform spectrum; in all other cases the numerically obtained frequency spectrum is shown. Model parameters to generate the driving signals are as stated in the main text, and the time scale parameters are $\tau_P = \tau_R = \tau_L = \tau_C = 1$. The probability density functions of the driving signals are displayed in insets (without axis annotations).

(R) *Rössler* driving, i.e., the first component of the (dimensionless) Rössler equations:

$$\dot{\tilde{x}} = -\frac{1}{\tau_R}(\tilde{y} + \tilde{z}), \quad \dot{\tilde{y}} = \frac{1}{\tau_R}(\tilde{x} + a\tilde{y}),$$
$$\dot{\tilde{z}} = \frac{1}{\tau_R}[b + \tilde{z}(\tilde{x} - c)]. \tag{5}$$

In the above equations we introduced parameter $\tau_R$ in order to control the time scale of the driving signal. With the common choice $a = 0.2$, $b = 0.2$, $c = 5.7$, the solution is chaotic. This way we realize randomlike driving, which is continuous in time. It can be viewed as a chaotically modulated periodic signal. For $\tau_R = 1$, its frequency spectrum [Fig. 3(b)] has a continuous background, governed by a power law of a large exponent for large frequencies. The crossover to this power law is commonly considered as the intrinsic time scale. In our case it is about $f \approx 1/5$. Over the continuous background of the frequency spectrum discrete peaks can be observed. The highest peak is associated with the principal periodic component, which is well visible in a time series (not shown). The reciprocal of the mean zero crossing time of the time series, 1/5.86, matches the principal peak frequency of the frequency spectrum very accurately, and hardly differs from the time scale extracted from the crossover in the spectrum. We choose therefore $f = 1/5.86$ as the characteristic frequency that leads to $\tau = 5.85\tau_R/4$. The mean of this driving signal is $\langle\tilde{x}(t)\rangle \approx 0.175$. In numerical simulations the equations of L84 and R are integrated in parallel using a fourth-order nonadaptive (fixed time step $h$) Runge-Kutta integrator. The fixed time step in any one integration is $h = 0.01$ or less.

(L) *Lorenz* driving, i.e., the first component of the (dimensionless) classical Lorenz equations:

$$\dot{\tilde{x}} = \frac{1}{\tau_L}\sigma(\tilde{y} - \tilde{x}), \quad \dot{\tilde{y}} = \frac{1}{\tau_L}(\rho\tilde{x} - \tilde{y} - \tilde{x}\tilde{z}),$$
$$\dot{\tilde{z}} = \frac{1}{\tau_L}(-\beta\tilde{z} + \tilde{x}\tilde{y}), \tag{6}$$

with the common choice $\sigma = 10$, $\rho = 28$, $\beta = 8/3$ for a chaotic solution. The frequency spectrum in Fig. 3(c) does not feature any obvious peak, only the continuous background. An initial slightly sloping plateau switches into a much more steep slope, which is also described by a power law but one of a much higher exponent (about 13). The location of the crossover appears to be the only feature based on which an intrinsic time scale can be defined. This occurs at frequency $f \approx 1.4$, which leads to $\tau = 0.7\tau_L/4$.

(C) *Red (colored) noise*, generated by the Ornstein-Uhlenbeck (OU) process, which is governed by the following (dimensionless) stochastic differential equation of the Langevin form:

$$\dot{\tilde{x}} = -\frac{1}{\tau_C}\tilde{x} + \sqrt{\frac{2}{\tau_C}}\xi, \tag{7}$$

where $\xi$ represents uncorrelated white noise,

$$\langle\xi(t_1)\xi(t_2)\rangle = \delta(t_1 - t_2) \tag{8}$$

($\delta$ denoting the Dirac delta) with a Gaussian distribution of zero mean and unit variance. The OU process realizes a Gaussian probability density distribution [see the inset in Fig. 3(d)]. Due to the bias, the first term on the right-hand side of Eq. (7), the variance of $\tilde{x}$ remains bounded.

Considering a well-known formula for the variance of the OU process [24], the strength of the white noise term $\xi$ is adjusted such that the variance of the process remains unity when varying $\tau_C$. Notice that rescaling time is not achieved simply by multiplying the right-hand side of the equation, contrary to drivings R and L.

The frequency spectrum of the OU process in Fig. 3(d) features a cutoff frequency $(2\pi\tau_C)^{-1}$, by which the length of the plateau can be approximated. We define the characteristic time scale of the process by the reciprocal of the plateau length, such as $\tau = 2\pi\tau_C/4$. It is noted that the case of white noise *of unit variance* is *not* obtained in the limit $\tau \to 0$.

For numerical solutions of the coupled L84 and OU equations an autonomous explicit order 1.5 strong scheme [25] has been used, which is detailed in the Appendix.

(W) Uncorrelated *white noise*:

$$\tilde{x} = \xi, \tag{9}$$

where $\xi$ has a Gaussian distribution of zero mean and unit variance, is also considered for reference. Due to a lack of

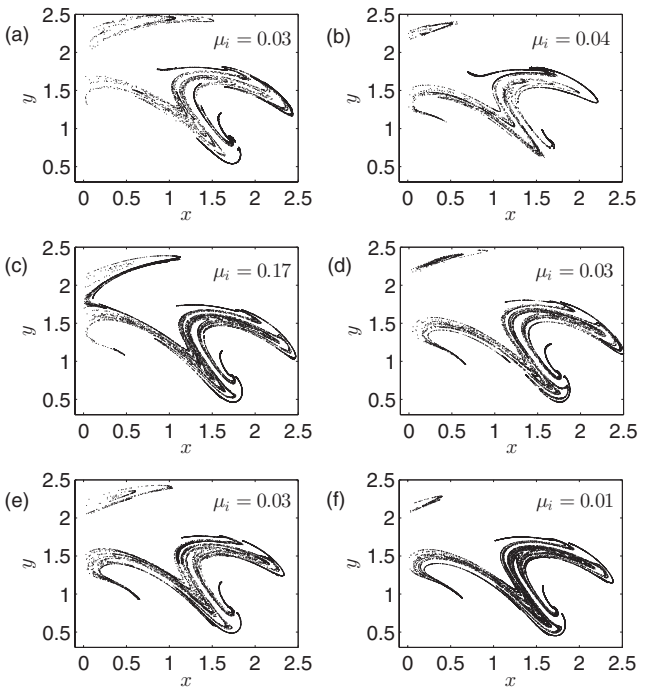


FIG. 4. Snapshot attractors on the Poincaré surface $z = 0, \dot{z} > 0$, of L84 driven by (a) P, a periodic signal ($A = 0.2797$), (b) R, the first component of the Rössler equations ($A = 0.0383$), (c) L, the first component of the classical Lorenz equation ($A = 0.025$), (d) C, red (colored) noise, i.e., OU driving ($A = 0.1978$), and (e) W, Gaussian white noise ($A = 0.1978$). (f) Chaotic attractor of the undriven L84 ($A = 0$, $F_0 = 8$). In all cases $\tau = 1$ is set. The snapshots are taken at the same time $t = 30$, and the instantaneous island measure (10) is also indicated. The time $t$ is measured from after 100 time units when the $N = 10^6$ trajectories, initially randomly distributed in $x, y \in [0,2]$, $z = 0$, already reached the snapshot attractor.

correlation there is no typical time scale associated with white noise, and hence it cannot be varied in this case. For numerical solutions, the same integrator scheme as described in the Appendix is applied.

In all cases the coupling strength $A$ is set so that $\Delta F = A\tilde{x}$ have the same variance, observing that the variance of $\tilde{x}$ for P, R, L, C, W are different. In case of the Lorenz driving L, $A = 0.025$ is set, which determines the settings of $A$ (different values) for all the other drivings. (For the particular values of $A$ refer to the figure caption of Fig. 4.) This setting implies relatively strong driving signals, which sweep ranges approximately as indicated by the double arrow in the bifurcation diagram of Fig. 2.

## III. SNAPSHOT ATTRACTORS

In the driven L84 system, when using a single trajectory, the attractor on the Poincaré surface is blurred. With an *ensemble* of chaotic trajectories, however, a clear 2D fractal snapshot attractor is obtained at any time instant. The geometry of the snapshot attractor changes over time [10].

Snapshot attractors can be numerically obtained using a cloud of initial conditions, all chosen from the same basin of attraction. After some time, the trajectories in the $(x, y, z)$ space attain the instantaneous three-dimensional (3D) snapshot attractor. When determining a 2D snapshot attractor taken on an appropriate Poincaré surface, one has to take into account that the ensemble of trajectories is necessarily of finite size in numerical studies. Thus, at any given time trajectory endpoints fall on the sectioning surface with zero probability. To cater for this, we proceed as follows. The unique time instants when the trajectories, each and every one, cross the surface are recorded, and those trajectories together are retained to form a PS whose crossing time fall in a particular time interval of length $\delta t \ll 1$. We used $\delta t = 0.02$. This window of time can subsequently be shifted in time to follow the time evolution of the PS of the snapshot attractor.

Examples of snapshot attractors are shown in Figs. 4(a)–4(e), one with each of the drivings described above. Intersection points with $\dot{z} > 0$ are considered only. The snapshot attractor consists of a "mainland," slightly displaced and distorted over time, and occasionally an "island" which can grow large, merge into the mainland, or disappear for finite periods of time. Thus, the island is identified as a feature in which the deviation of the driven system from the undriven one is clearly manifested, since in the latter a medium size island is permanently present (see the scattered points around $y = 2$ in Fig. 2). The islands represent large $y$ values. In physical terms they correspond to *extreme* or strong cyclonic activity. Therefore the extremal behavior of this type of cyclonic activity is of particular interest.

The island measure $\mu_i$ is considered to be the proportion of the number of points that make up the island. In order to deal with cases when the island merges into the mainland, we apply as a practical definition the proportion of points that satisfy the condition $y > 1.9$:

$$\mu_i = \mu(y > 1.9 | z = 0). \tag{10}$$

As an example, the time series of the island measure corresponding to Fig. 4(c) is shown in Fig. 5(a). The upper horizontal line indicates the maximal island size of all those undriven systems for which the constant $F$ is from the range of the double arrow of Fig. 2. (Regular regimes where no islands exist are represented by $\mu_i = 0$.) It is perhaps the most remarkable feature of the diagram that the maximal value $\mu_i = 0.044$ (for about $F \equiv 8.33$) is exceeded regularly and significantly [26]. The lower horizontal line indicates the island size for $F \equiv 8$.

It has been demonstrated [16] by numerically obtaining the probability density distributions over snapshot attractors that the excessive island measures are due not only to the grown extent of the island, but also to occasionally much increased probabilities. This intermittent behavior becomes more frequent and characteristic, or, indeed, the accumulation of points, due to the reduction or sign change of the local maximal Lyapunov exponent [27], becomes the rule rather than the exception as a change of parameter (e.g., reducing $F_0$ in our case) shifts the driven system towards regular dynamics. A much more characteristic intermittent behavior has been found in a low-order El Niño–Southern Oscillation (ENSO) model [14].

Another measure $\mu_c$ to consider extreme cyclonic activity is the measure

$$\mu_c = \mu(r > 1.8) \tag{11}$$

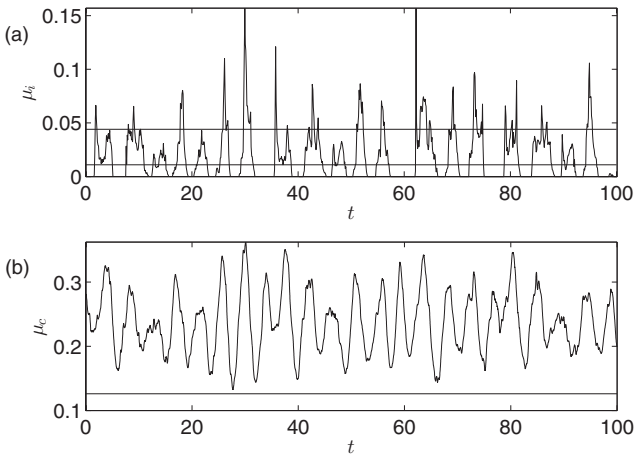


FIG. 5. Time series of (a) the island measure (10) of the 2D- and (b) the cyclonic activity measure (11) of the 3D snapshot attractors using the Lorenz driving ($\tau = 1, F_0 = 8, A = 0.025$). An ensemble of $10^6$ trajectories is used. Horizontal lines indicate the reference values in terms of the undriven system: (a) $\mu_i = 0.01$ at $F \equiv 8$, maximal $\mu_i = 0.044$ at $F \equiv 8.33$, and (b) $\mu_c = 0.126$ at $F \equiv 8$.

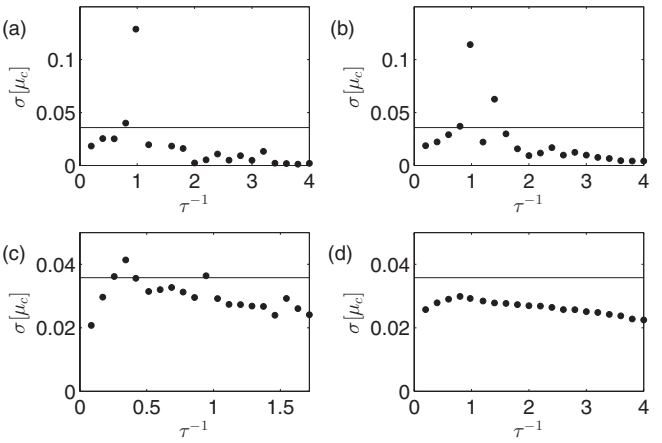


FIG. 6. Dependence of $\sigma[\mu_c]$ on $\tau^{-1}$ for various drivings: (a) P, (b) R, (c) L, and (d) C. For reference, a horizontal line indicates $\sigma[\mu_c] = 0.036$ for the Gaussian white noise-driven case. Note the different range for $\tau^{-1}$ in case of the Lorenz driving (L), and the different range for $\sigma[\mu_c]$ in case of L and C.

of that part of the 3D snapshot attractor that satisfies the condition $r > 1.8$. Since $r$ is defined by (2), this condition allows for large values in either $y$ or $z$ (or both). The time-dependent $\mu_c(t)$ can be interpreted as a measure of the likelihood or probability of strong cyclonic activities at any time. It is computationally much more efficient to determine $\mu_c$ than $\mu_i$. In fact, there is a correlation between the two, as testified by Fig. 5. The maximal value of the cross-correlation function is about 0.6.

It is worth emphasizing that for the range of parameters investigated the snapshot attractor is never found to be regular in spite of the fact that the $F$ values cover several periodic windows of the undriven problem. Regular behavior is thus suppressed by driving. This has been explained [5] in terms of transiently chaotic dynamics in the periodic windows of the undriven system, namely, that the relatively fast driving does not allow the trajectories to settle on, or even to closely approach, the regular attractor before they are driven back to chaotic parameter regimes. The consistent geometry of the snapshot attractors is due to the fact that in the periodic window the nonattracting chaotic sets, or their unstable manifolds, resemble the attractors of neighboring chaotic regimes.

## IV. ENHANCEMENT OF EXTREMES

In the following the different types of driving described in Sec. II will be analyzed by varying their time scales. Their effect on three different scalar indicators of extremal behavior will be considered. The first one is described in the snapshot attractor framework, and the second and third ones in a single trajectory framework. At the end of the section we return to the snapshot attractor framework and consider the case of periodic driving, which will help in interpreting the main finding: a resonancelike enhancement of the magnitude and variability of extremes.

### A. Measure of strong cyclonic activity

The first indicator to be considered is the measure $\mu_c$ of strong cyclonic activity, defined in Sec. III. The $\tau$-dependence of the variance, or standard deviation $\sigma[\mu_c] = \langle(\mu_c - \langle\mu_c\rangle)^2\rangle^{1/2}$, is shown in Fig. 6. Note that $\tau^{-1}$ is measured on the horizontal axis, in a fashion similar to frequency spectra (as in Fig. 3). To obtain a time series for $\mu_c$, $N = 10^5$ randomly initialized trajectories were followed for 300 time units, all subject to the same perturbation, after an initial simulation of 300 time units. We make the following observations:

(i) For all types of driving $\sigma[\mu_c]$ is enhanced relative to the undriven case of zero $\sigma[\mu_c]$. (ii) The dependence of $\sigma[\mu_c]$ on $\tau^{-1}$ is nonmonotonic and features a maximum. (iii) The more regular the driving, exhibiting a higher degree of periodicity, the more characteristic the maximum. (iv) The maxima occur when the characteristic time scale of the drivings is on the order of that of L84, i.e., when $\tau$ is of order 1. (v) For very short time scales the undriven case is approached, i.e., $\sigma[\mu_c] \to 0$ as $\tau \to 0$. (vi) The more irregular the driving, this convergence becomes the slower. (vii) The enhancement with white noise driving can be exceeded around the local maxima.

Points (i)–(iv) describe an effect which may be interpreted as a kind of *resonance*. It is convenient to shift all resonances to $\tau \approx 1$. To this end we rescale the dimensionless time with the Lorenz driving and choose a $\tau'$ as $\tau' = 2.33\tau = 1.63\tau_L/4$.

Point (v) is expected on the basis of stochastic singular perturbation theory [28–30]. The technique of stochastic mode reduction is based on this theory, with the following premise. The strength $\sigma_\xi$ of the equivalent white noise to some relatively fast time-continuous driving signal $\tilde{x}(t)$ is proportional to the total integral of the autocorrelation function of the latter. This reads formally as follows:

$$\sigma_\xi \propto \int_0^\infty \left[ \lim_{T\to\infty} \int_0^T \tilde{x}(s)\tilde{x}(t+s)ds \right] dt. \qquad (12)$$

$\tau$ compares well with the time scale of the decay of the autocorrelation function (in the square brackets above), and so the area below it, with which $\sigma_\xi$ is proportional, vanishes

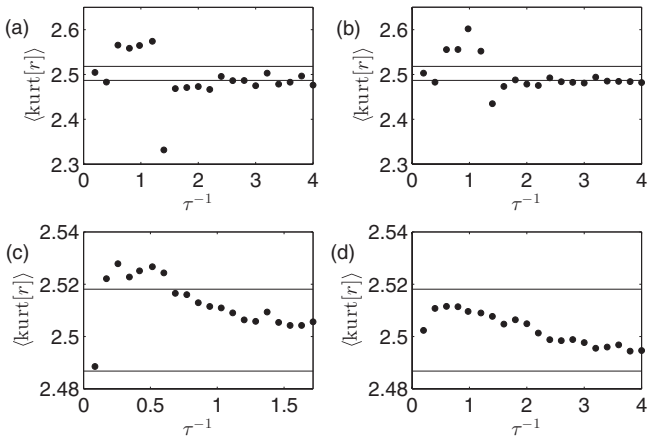


FIG. 7. Kurtosis of distributions of $r$ vs $\tau^{-1}$ for various drivings: (a) P, (b) R, (c) L, and (d) C. For reference, two horizontal lines indicate figures for the undriven case (lower) and for the Gaussian white noise-driven case (upper).

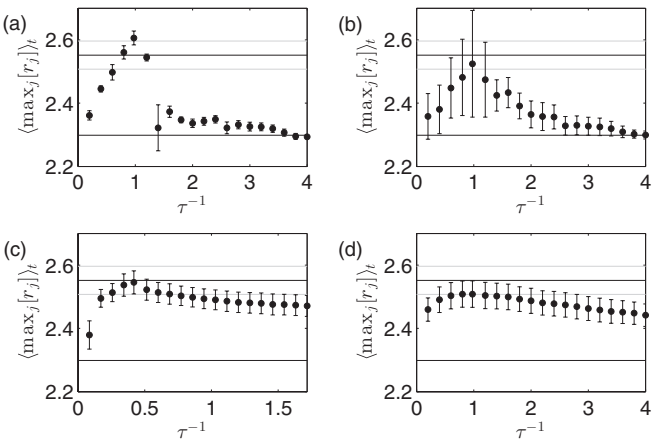


FIG. 8. Dependence of a robust estimator of the maximal extreme value $r_{\max}$ on $\tau^{-1}$ for various drivings: (a) P, (b) R, (c) L, and (d) C. Solid circles (•) and corresponding error bars indicate the mean $\langle \max_j[r_j] \rangle_t$ and standard deviation $\sigma_t[\max_j[r_j]]$, respectively. For reference, the lowest horizontal black line indicates $\max[r] = 2.30$ for the undriven case. Another reference is provided in terms of the Gaussian white noise-driven case: the upper horizontal black line (at $r = 2.55$) corresponding to the solid circles, and the pair of horizontal gray lines corresponding to the error bars.

as $\tau \to 0$. Therefore, despite that numerical results in Fig. 6 have been produced over a rather limited range of $\tau$, we expect that the observed vanishing tendencies continue for $\tau^{-1}$ or $\tau'^{-1} > 4$.

### B. Kurtosis

Next we consider the total cyclonic activity $r$ (2) in a single trajectory framework. The kurtosis of the probability density distribution of variable $r$, $\langle \text{kurt}[r] \rangle$, is shown in Fig. 7. Time series of $r$ of length 5000 time units are considered for this. A number of $N = 100$ different realizations of the drivings have been used to obtain the average over the realizations: $\langle \text{kurt}[r] \rangle \equiv \langle \text{kurt}[r_j] \rangle_j$, $j = 1, \ldots, N$. The standard deviation of the estimator is obtained as $\sigma_j[\text{kurt}[r_j]]/\sqrt{N}$. With $N = 100$ this yields such small figures that error bars are comparable in size with the marker size, and so they are not featured in the diagrams. For reference, baselines of kurt$[r]$ of the undriven case (lower) and the white noise-driven case (upper) are included. Observations (i)–(vii) as detailed above apply to the kurtosis, too. This implies that the maxima of $\langle \text{kurt}[r] \rangle$ coincide with those of $\sigma[\mu_c]$.

### C. Maximal extreme value

A simple indicator of extremes is the maximal extreme value that a variable can take. This maximum, $r_{\max}$, can be approximated from below by the maximal element of a very long time-series $r(t)$, denoted by $\max[r]$. Equivalently, in a numerical procedure, using an ensemble of trajectories $r_j(t)$, $j = 1, \ldots, N$, $r_{\max}$ can be approximated by the maximal element of the all-time maximal element of the ensemble of much shorter time series: $\max_t[\max_j[r_j(t)]]$.

We found that more robust indicators of tendencies with respect to the time scale of driving $\tau$ are given by the mean $\langle \max_j[r_j] \rangle_t$ and standard deviation $\sigma_t[\max_j[r_j]]$, which are shown in Fig. 8 by solid circles (•) and error bars, respectively. For these results we used $N = 10^4$ randomly initialized and independently driven trajectories, and followed them over 300 time units, after an initial run of 300 time units.

The same observations (i)–(vii) made above in the case of $\sigma[\mu_c]$ apply to $\langle \max_j[r_j] \rangle_t$, too. This implies that the maxima of $\langle \max_j[r_j] \rangle_t$ coincide with those of $\langle \text{kurt}[r] \rangle$ and $\sigma[\mu_c]$. That this is not a mere coincidence is indicated in Sec. IV D.

The enhancement may be interpreted as a resonancelike effect. It is noted, however, that an enhancement is observed only in $\langle \max_j[r_j] \rangle_t$, but the variance, or $\langle \sigma_t[r_j] \rangle_j$, has not been found to vary with $\tau$ to a measurable degree. It is also noted that $\langle \max_j[r_j] \rangle_t$ is enhanced maximally by just over 10%.

The phenomenon of resonance is traditionally associated with linear systems driven by periodic signals. Here we find that an enhancement of extremes typically occurs in nonlinear systems driven by aperiodic signals or noise. This effect is the strongest when an average period of the driving exists, and it is comparable with the characteristic time scale of the undriven system. It is not surprising that the amount of enhancement of, e.g., the maximal value is found to be smaller in such cases than in the classical setting.

### D. Island measure with periodic driving

When the driving is periodic, $\mu_c(t)$ or $\mu_i(t)$ are also periodic, despite the chaotic individual constituent trajectories in the ensemble from which the measures are estimated. This is due to the fact that a stroboscopic Poincaré map exists in this case, the attractor of which is equivalent with the 3D snapshot attractor, as discussed in Ref. [5]. Therefore, e.g., $\max[\mu_i]$ can be estimated as soon as the ensemble converges to the snapshot attractor—whereas with an irregular driving the estimation of $\max[\mu_i]$ with the same accuracy might be possible only from a much longer time series $\mu_i(t)$, which is proportionally more demanding to generate numerically. This is why $\mu_i$ is not considered in Sec. IV A. In the periodic case, however, it is affordable and also insightful to consider.

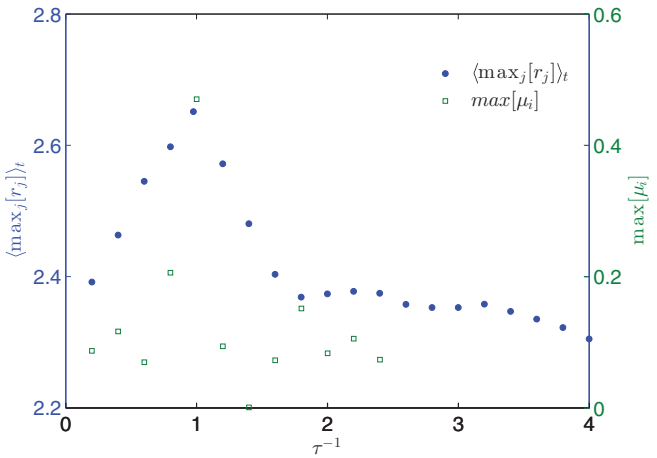


FIG. 9. (Color online) Dependence of $\max[\mu_i]$ and $\langle \max_j[r_j]\rangle_t$ on $\tau^{-1}$ for L84 driven periodically ($F_0 = 8$, $A = 0.2797$).

In Fig. 9 $\max[\mu_i]$ is shown, along with $\langle \max_j[r_j]\rangle_t$, depending on $\tau^{-1}$. We observe a sharp peak of $\max[\mu_i]$ just about the peak of $\langle \max_j[r_j]\rangle_t$. At this time scale of the driving $\mu_i \approx 1/2$, i.e., the island is comparable in weight with the mainland. In a detailed numerical study, resolving $\tau$ very finely, for several distinct values around $\tau = 1$, some attracting period-3 and period-8 cycles have been found (not shown). That is, by some periodic driving, a chaotic trajectory of L84 can be turned into a periodic cycle—a phenomenon referred to as *resonant chaos control* [31]. It has been demonstrated in Ref. [31] that an unstable periodic orbit (UPO) of the chaotic attractor can be stabilized by adding harmonic driving, whose frequency is adjusted to that of the UPO, and whose amplitude is also adjusted appropriately. The UPOs that can be most readily stabilized in this simple way are those *in association* with neighboring periodic windows of a bifurcation diagram. As in our case the amplitude was not adjusted, it is more likely that the resulting periodic cycles can be *approximated* by periodic cycles from neighboring periodic windows [32].

Thus, the enhanced magnitude of extremes and variance $\sigma[\mu_c]$ can be explained in a way that at relative frequencies closer to unity ($\tau \approx 1$) the periodic perturbation retains more of its stabilizing power. Time to time conditions are favorable to regularize parts of the snapshot attractor (by locally decreasing the instability, i.e., the maximal Lyapunov exponent of trajectories), which manifests itself in the accumulation, i.e., synchronization of trajectories. This mechanism works in a similar manner in the case of irregular drivings, but suitable conditions for synchronization occur less often, which is reflected in, e.g., a more modest enhancement of $\sigma[\mu_c]$ for L as opposed to P in Fig. 8.

In the light of (temporarily) stabilized and *regularized* trajectories the effect of enhanced kurtosis can also be explained. The distribution of the highly regular periodic signal is peaked at the extremes or turning points [see the inset of Fig. 3(a)], because turning takes more time than crossing the mean value, and turning takes place always at the same turning point. Such a distribution has a large kurtosis, which measures the relative frequency of large and extreme values of the variable.

## V. EXTREME VALUE STATISTICS

Extreme value statistics (EVS) characterizes the tail of the probability density distribution of a variable. This is important if expected return times of dangerous extremes are to be determined. According to a common approach, the maximal elements of large blocks of $n$ consecutive data points of a discrete time series are considered. The time evolution of $r$ in our case is continuous, and so discrete data points will be defined by the local maxima or turning points of $r(t)$ [33]. The turning points follow each other irregularly in time, nevertheless, for large $n$ the statistics (i.e., parameters of the fitted distribution) may converge. As an example, probability density distributions of maximal elements in blocks of length $n = 1000$ are displayed in Fig. 10.

According to classical extreme value theory, probability distributions of the block maxima of some random variable $x$, which are well behaved in the asymptotic limit $n \to \infty$, can be described by a three-parameter $(\mu,\sigma,\xi)$ family of *generalized extreme value* (GEV) distributions:

$$G(x;\mu,\sigma,\xi) = \exp\left\{-\left[1+\xi\left(\frac{x-\mu}{\sigma}\right)\right]^{-1/\xi}\right\}, \quad (13)$$

which combines the Gumbel ($\xi \to 0$), Fréchet ($\xi > 0$), and Weibull ($\xi < 0$) families [34]. In the case of one-dimensional chaotic systems, Nicolis and co-workers [19] claim that the distribution of block maxima has discontinuities for any $n$, and related features might also show up in multidimensional systems [20]. Fereitas *et al*. [23] showed that it is nevertheless

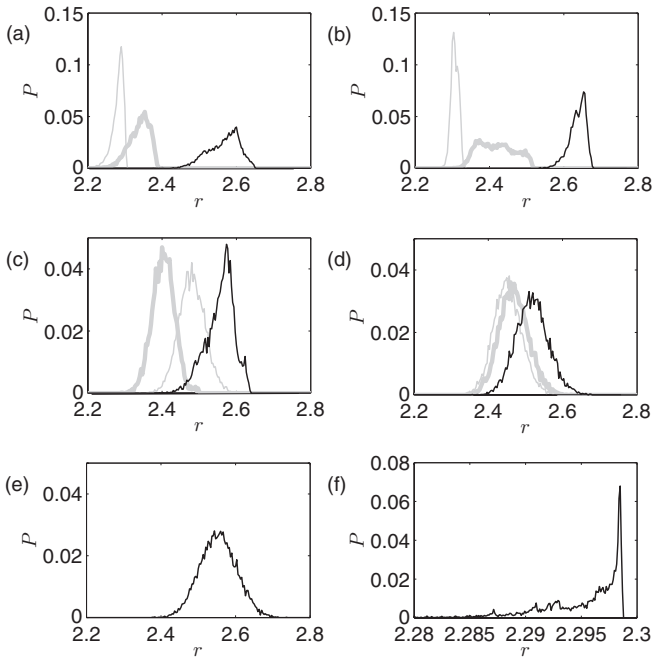


FIG. 10. Distribution (histogram) $P = P(r)$ of maximal elements of $r$ in blocks of $n = 1000$ consecutive maxima of $r(t)$. For each driving, (a) P, (b) R, (c) L, and (d) C, three values of $\tau$ ($\tau'$ for L) are used, such as $\tau^{-1} = 0.2$ (thick gray line), 1 (black), 4 (thin gray), that is, the smallest and largest, and an approximately resonant sample value of $\tau$ from Fig. 8. For each histogram a number of 300 bins are used between [2, 3], except for the case of the undriven L84, when the histogram is concentrated over a much shorter range.

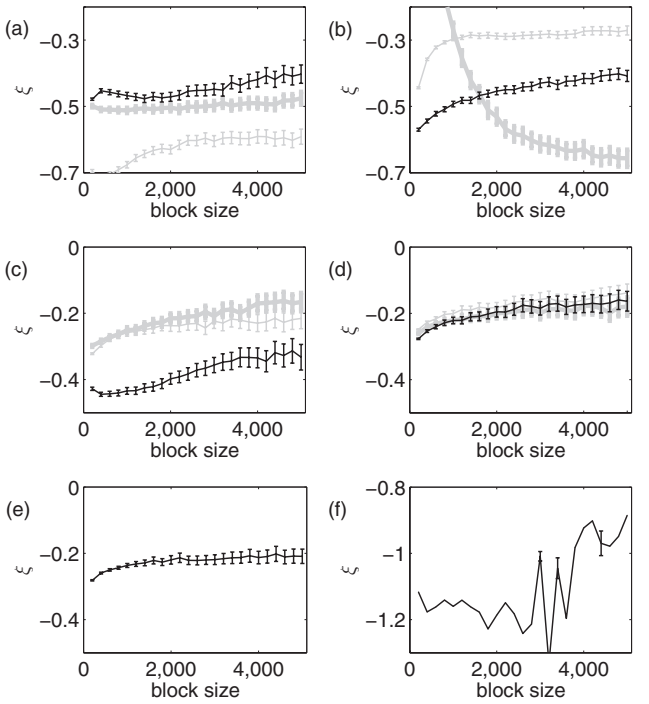


FIG. 11. Estimates of the shape parameter $\xi$ of the GEV distribution, corresponding with Fig. 10: (a) P, (b) R, (c) L, and (d) C. The error bars indicate the 95% confidence interval of estimation.

meaningful to fit a smooth GEV distribution (13) even in this case, because the shape parameter ($\xi$) of the best fitting GEV distributions may converge to a well defined limit value as $n \to \infty$. We adopt this approach in the following (for a discussion of this issue see also Ref. [35]).

Given a fixed amount of data, a trade-off situation presents itself between the accuracy and bias of estimation, these being functions of the used block size $n$. For this reason it is common to do the estimation procedure iteratively by gradually increasing the block size [36]. The original time series has to be long enough that an approximation of the limit $n \to \infty$ be possible with relatively small errors. For our analysis we generated a number of about $10^7$ maxima, with which an iterative estimation of the shape parameter (increasing the block size up to $n = 5000$) resulted in the diagrams shown in Fig. 11. These figures are all consistent with Weibull distributions.

It is interesting to note that the shape parameter remains negative also for the white noise driving. In principle, $\Delta F(t)$ in this case can take on arbitrary large values (and should be consistent with a Gumbel-type extreme value distribution). The probability of such events is, however, so small that they typically do not occur during the time periods of observations used here. This observation justifies the use of Gaussian white noise for mimicking a random driving of finite amplitude in Eq. (9) *a posteriori*. The same remark applies also to the red noise driving, which results in similarly small values of $|\xi|$, indicating extended tails. As a rule, deterministic drivings tend to result in somewhat larger values of $|\xi|$, corresponding to more bulky tails.

The undriven case is rather special from the point of view of the shape parameter. As panel (f) shows, the values are around $\xi = -1$, which implies a sharp discontinuous edge of the distribution. There is no sign of convergence in the region shown. This is not a surprise since it is known [34] that estimators of the shape parameters $\xi < -1$ are generally not obtainable by maximum likelihood estimation, and estimators of $-0.5 < \xi < -1$ have no standard asymptotic properties. If the actual edge is sharp but continuous, the shape parameter $\xi$ should be greater than $-1$. This cannot be verified by the numerical results. However, there is another way of determining $\xi$ in this case. The theoretical value of $\xi$ is believed to be obtainable by the following formula [21]: $-1/\xi = D_0^{(1)}/2 + D_0^{(2)}$, where the Hausdorff dimension of the attractor on some smooth surface, along the unstable manifold, is $D_0^{(1)} = 1$, and $D_0^{(2)}$ denotes that along the stable manifold [37]. We estimated the fractal dimension $D_0$ on the $z = 0$ Poincaré surface, applying a 2D box-counting algorithm on $10^5$ points, to be $D_0 \approx 1.6$, with which $D_0^{(2)} = D_0 - D_0^{(1)} \approx 0.6$. This implies that $\xi \approx -0.9$.

It is meaningful to ask whether a similar resonancelike effect as discussed in Sec. IV [point (iv)] exists also in terms of $\xi$. We observe in Fig. 11 that the order of the curves for different values of $\tau$ is different with the different drivings. Thus, no resonance exists in terms of $\xi$. Without this, a similar rule to point (vi) can certainly not hold either, and so, interestingly, the two chaotic drivings (R and L) differ from each other as much as either of them differs from the highly regular periodic driving. It can be said, thus, that the shape parameter depends strongly on the individual driving signal.

## VI. CONCLUSIONS

In this paper we examined the effects of drivings with variable time scale on the extremal behavior of a model climate system, Lorenz's 1984 model of global atmospheric circulation. Several measures of extremal behavior have been considered, such as the maximal extreme value, the relative frequency of extreme events in terms of the kurtosis, and the shape parameter of the extreme value distribution. Beside these measures defined in a single trajectory framework, we also considered the likelihood of extreme events in a snapshot attractor framework, in particular, in terms the likelihood of strong cyclonic activities, defined as a measure of the 2D or 3D snapshot attractor.

The main finding of this work is that the above measures of extremes (except the shape parameter) are typically not reduced but *enhanced* upon introducing some driving, and that their enhancement is maximal when the characteristic time scale of the driving is on the order of that of the climate system. This resonance-like effect is interpreted in terms of the periodically driven case, referring to the technique of resonant chaos control. The driving can enhance the stability of trajectories.

Using the various types of driving of equal variance, the extent of maximal enhancement of the maximal extreme value have been found to be comparable. This applies also to the maximal enhancement of the kurtosis. We find it interesting that the white noise driving is no exception in this regard, since it is often viewed as a fast driving, and other fast time-continuous drivings appear to have vanishing impact.

The impact of the various drivings on the extreme value distribution has been also studied. The shape parameter tends to be smaller in modulus for stochastic drivings. Otherwise, the shape parameter strongly depends on the individual type of driving (i.e., shape and variance of distribution, and correlation properties such as the characteristic time scale). In this regard, future work should be concerned with the impact on the predictability of extremes in driven model systems when some driving, other than the original one, is used.

When comparing the magnitude and variability of extremes around the resonance frequency, we find that the effect of deterministic drivings is more pronounced than any of the stochastic drivings. The largest maxima belong to the exactly periodic driving, but such a driving is unrealistic in the climatic context. The most pronounced effect is thus expected to belong to chaotic drivings with some superimposed periodic components, such as the Rössler model. It is interesting to observe that although red noise is generally considered to better approximate chaos than white noise, the red noise results remain below the level of white noise results, and the latter are exceeded by the effects of the deterministic driving around resonance. A moral from this study could be that the widest range of extremes are generated by driving via structured deterministic noise, i.e., by chaotic driving exhibiting a certain degree of periodicity as well.

## ACKNOWLEDGMENTS

Valuable comments by M. Ghil, K. Fraedrich, H. Kantz, and I. M. Jánosi are gratefully acknowledged. T.B. is grateful for support through a postdoctoral fellowship given by the Max Planck Society, and T.T. for support from the Alexander von Humboldt Foundation. This work was supported by the Hungarian Science Foundation under Grant No. NK100296. The project is also supported by the European Union and is cofinanced by the European Social Fund (Grant Agreement No. TAMOP 4.2.1./B-09/KMR-2010-0003).

## APPENDIX: STOCHASTIC NUMERICAL INTEGRATOR SCHEME

The implemented autonomous explicit order 1.5 strong scheme [25] is suitable in the case of diagonal noise (single independent noise terms appearing in each component). The system of a number of $d$ coupled stochastic differential equations is assumed to take a form such as $\dot{Y} = a(Y) + b\xi$, where $Y = \{Y^k\}$, $a = \{a^k\}$, $b = \{b^{k,l}\}$, $\xi = \{\xi^k\}$, $k,l = 1, \ldots, d$. When $b$ is a constant diagonal matrix (in our case only one element is nonzero along the diagonal), the integrator scheme reads as follows:

$$Y_{n+1}^k = Y_n^k + b^{k,k}\Delta W^k + \frac{1}{2\sqrt{h}}\sum_{j=1}^{d}\{a^k(\bar{Y}_+^j) - a^k(\bar{Y}_-^j)\}\Delta Z^k + \frac{h}{4}\sum_{j=1}^{d}\left\{a^k(\bar{Y}_+^j) - \frac{2(d-2)}{d} + a^k(\bar{Y}_-^j)\right\}, \tag{A1}$$

where

$$\bar{Y}_\pm^j = Y_n + \frac{1}{m}ah \pm b^k\sqrt{h}, \tag{A2}$$

$$\Delta W^k = \xi_1^k\sqrt{h}, \tag{A3}$$

$$\Delta Z^k = h^{3/2}/2\left(\xi_1^k + \xi_2^k/\sqrt{3}\right), \tag{A4}$$

in which $\xi_1^k$'s and $\xi_2^k$'s are independent uniformly distributed random variables of zero mean and unit variance. For satisfactory accuracy of the numerical solution, time step $h$ must be much smaller than the shortest time scale of the deterministic dynamics determined by $a(Y)$.

[1] J. von Neumann, in *Dynamics of Climate*, edited by R. L. Pfeffer (Pergamon, Oxford, UK, 1960).
[2] *Climate Change 2007: Synthesis Report. Contribution of Working Groups I, II and III to the Fourth Assessment Report of the Intergovernmental Panel on Climate Change*, edited by IPCC Core Writing Team, R. K. Pachauri, and A. Reisinger (IPCC, Geneva, Switzerland, 2007).
[3] K. Hasselmann, Tellus **28**, 473 (1976).
[4] Talk given by R. T. Pierrehumbert at SIAM Conference on the Application of Dynamical Systems, Snowbird, 2011 (unpublished).
[5] T. Bódai and T. Tél, Chaos **22**, 023110 (2012).
[6] Talk given by S. Stainforth at the Climate Sensitivity session of the EGU2012 meeting, Vienna, 2012 (unpublished).
[7] M. Ghil, Alfred Wegener Medal Lecture, EGU2012 meeting, Vienna, 2012 (unpublished), http://www.cntv.at/EGU2012/index.php?modid=18&a=show&pid=190.
[8] L. Arnold, *Random Dynamical Systems* (Springer, Berlin, 1998).
[9] F. J. Romeiras, C. Grebogi, and E. Ott, Phys. Rev. A **41**, 784 (1990).
[10] F. Ledrappier and L.-S. Young, Commun. Math. Phys. **17**, 529 (1988).
[11] G. R. Sell, Trans. Amer. Math. Soc. **127**, 241 (1967).
[12] M. Ghil, M. D. Chekroun, and E. Simonnet, Physica D **327**, 2111 (2008).
[13] *Stochastic Physics and Climate Modelling*, edited by T. N. Palmer and P. Williams (Cambridge University Press, Cambridge, UK, 2010).
[14] M. D. Chekroun, E. Simonnet, and M. Ghil, Physica D **240**, 1685 (2011).
[15] T. Bódai, G. Károlyi, and T. Tél, Phys. Rev. E **83**, 046201 (2011).
[16] T. Bódai, Gy. Károlyi, and T. Tél, Nonlinear Processes Geophys. **18**, 573 (2011).
[17] E. N. Lorenz, Tellus **36A**, 98 (1984).
[18] A. Provenzale and N. J. Balmford, *Chaos and Structures in Geophysics and Astrophysics* (Woods Hole Oceanographic Institution, Woods Hole, MA, 1999), http://www.whoi.edu/fileserver.do?id=21476&pt=10&p=17353.
[19] C. Nicolis, V. Balakrishnan, and G. Nicolis, Phys. Rev. Lett. **97**, 210602 (2006).
[20] C. Nicolis and G. Nicolis, Phys. Rev. E **85**, 056217 (2012).

[21] M. P. Holland, R. Vitolo, P. Rabassa, A. E. Sterk, and H. W. Broer, Physica D **241**, 497 (2012).
[22] D. Faranda, V. Lucarini, G. Turchetti, and S. Vaienti, J. Stat. Phys. **145**, 1156 (2011).
[23] A. C. M. Freitas, J. M. Freitas, and M. Todd, Probab. Theory Relat. Fields **147**, 675 (2010).
[24] D. Henderson and P. Plaschko, *Stochastic Differential Equations in Science and Engineering* (World Scientific, Singapore, 2006).
[25] P. E. Kloeden and E. Platen, *Numerical Solution of Stochastic Differential Equations* (Springer, Berlin, 1995).
[26] Defining an island by $y > 1.9$ results in a maximal island "measure" of $1/13 = 0.077$ for the dominant period-13 attractor in the periodic window. This value is also exceeded by far.
[27] L. Yu, E. Ott, and Q. Chen, Phys. Rev. Lett. **65**, 2935 (1990).
[28] R. Z. Khasminsky, Theory Probab. Its Appl. **11**, 211 (1966).
[29] C. Franzke and A. J. Majda, J. Atmos. Sci. **63**, 457 (2006).
[30] L. Mitchell and G. A. Gottwald, J. Atmos. Sci. **69**, 1359 (2012).
[31] M. Kraus, J. Müller, D. Lebender, and F. W. Schneider, Chem. Phys. Lett. **260**, 51 (1996).
[32] A. Hübler and E. Lüscher, Naturwissenschaften **76**, 67 (1989).
[33] This also relaxes data storage requirements in numerics.
[34] S. Coles, *An Introduction to Statistical Modeling of Extreme Values* (Springer, Berlin, 2001).
[35] M. Ghil, P. Yiou, S. Hallegatte *et al.*, Nonlinear Processes Geophys. **18**, 295 (2011).
[36] P. Embrechts, C. Klüppelberg, and T. Mikosch, *Modelling Extremal Events for Insurance and Finance* (Springer, Berlin, 1997).
[37] In Eqs. (1) and (2), the complete set of the upper turning points $\{r_i = r(t = t_i) : \dot{r}(t_i) = 0\}$ define an $f(x,y,z) = 0$ Poincaré section (PS) of the 3D attractor of the undriven system. The shape parameter of the extreme vale distribution of the $r_i$'s are determined by the fractality of this PS, or equivalently that of any other PS $g(x,y,z) = 0$ that can be continuously mapped onto $f(x,y,z) = 0$.